Design, fabrication, and characterization of a planar, silicon-based, monolithically integrated micro laminar flow fuel cell with a bridge-shaped microchannel cross-section

P.O. López-Montesinos [a,b], N. Yossakda [c], A. Schmidt [a], F.R. Brushett [a,b], W.E. Pelton [c], P.J.A. Kenis [a,b,*]

[a] Department of Chemical & Biomolecular Engineering, University of Illinois at Urbana-Champaign, 600 S. Mathews Avenue, Urbana, IL 61801, USA
[b] Beckman Institute for Advanced Science and Technology, 405 N. Matthews Avenue, Urbana, IL 61801, USA
[c] Finesse Inc., 44870 Osgood Road, Fremont, CA 94539, USA

ARTICLE INFO

ABSTRACT

We report the fabrication of a planar, silicon-based, monolithically integrated micro laminar flow fuel cell (μLFFC) using standard MEMS and IC-compatible fabrication technologies. The μLFFC operates with acid supported solutions of formic acid and potassium permanganate, as a fuel and oxidant respectively. The micro-fuel cell design features two *in-plane* anodic and cathodic microchannels connected via a bridge to confine the diffusive liquid–liquid interface away from the electrode areas and to minimize crossover. Palladium high-active-surface-area catalyst was selectively integrated into the anodic microchannel by electrodeposition, whereas no catalyst was required in the cathodic microchannel. A three-dimensional (3D) diffusion-convection model was developed to study the behavior of the diffusion zone and to extract appropriate cell-design parameters and operating conditions. Experimentally, we observed peak power densities as high as 26 mW cm^{-2} when operating single cells at a flow rate of 60 μL min^{-1} at room temperature. The miniature membraneless fuel cell design presented herein offers potential for on-chip power generation, which has long been prohibited by integration complexities associated with the membrane.

© 2011 Elsevier B.V. All rights reserved.

1. Introduction

Small, portable consumer electronics such as mobile phones, laptop computers, personal digital assistants, and global-positioning systems, have recently merged into single platforms and gained superior multitasking abilities in part enabled by major advances in wireless communication and data transmission [1]. The high resolution capability, batch production, and reproducibility accessible via microfabrication technologies for integrated circuits (IC) and microelectromechanical systems (MEMS) enable further miniaturization and integrated-device sophistication in a cost-effective manner [2,3]. Moreover, the next generation of MEMS, *i.e.,* sensors, actuators, and lab-on-a-chip devices, are expected to operate remotely to accomplish particular machine-enhanced human endeavors in the diverse arenas of medicine, environmental sciences and engineering [4–6]. Miniaturized secondary (rechargeable) batteries such as Ni–Cd, Li-ion, and Li-polymer, while presently powering the vast majority of portable devices,

may no longer feature the necessary energy density to cope with these new power demands and required device autonomy [7]. As an alternative, MEMS-based electrochemical energy converters such as micro-fuel cells (μFCs), particularly intended to operate with easily handled and stored liquid fuels (*e.g.,* methanol, formic acid), are envisioned as a possible solution due to their high energy density, efficiency, and quasi-instant recharge capability by easy reactant refilling [8–10].

Silicon-based μFCs offer the possibility of parallel integration with other electronic components on the same chip [11]. On-chip integration requires a compact μFC architecture that can be fabricated using standard MEMS/IC-compatible (*i.e.,* CMOS-compatible) technologies [12]. After the first silicon-based miniature fuel cell was reported [3], numerous researchers have pursued the miniaturization of the traditional proton-exchange membrane fuel cell (PEMFC) bilayer design, composed of two bipolar substrates for the delivery of reactants and current collection clamped to a membrane-electrode assembly (MEA) [7]. To complete this complex multicomponent structure, hybrid integration using non-standard fabrication techniques (*e.g.,* catalyst painting, hot pressing, hot rolling) is required [8]. As an alternative, Maynard and Mayers proposed a micro-fuel cell architecture with anodic and cathodic channels formed on a single silicon substrate [13]. The use of a single substrate facilitates monolithic integration in

* Corresponding author at: Department of Chemical & Biomolecular Engineering, University of Illinois at Urbana-Champaign, 600 S. Mathews Avenue, Champaign, IL 61801, USA. Tel.: +1 217 265 0523; fax: +1 217 333 5052.
E-mail addresses: kenis@illinois.edu, kenis@uiuc.edu (P.J.A. Kenis).

a layer-by-layer, build-etch sequence using MEMS/IC-compatible technologies. Modeling of this planar miniature fuel-cell revealed that it is a less effective alternative than the bilayer (bipolar) architecture, primarily due to surface-area penalties [14]. However, IC-compatible electrodeposition techniques to integrate high-active-surface-area catalysts [15,16] and surface texturing methods [17] have recently been documented. For instance, Motokawa et al. [18] demonstrated single-cell performance of a MEMS-based micro-direct-methanol fuel cell (μDMFC) based on the aforementioned principles. Table 1 summarizes efforts pertaining to the development of monolithic μFCs for on-chip integration as reported in the literature. Despite major advances in system integration and associated performance, on-chip implementation of fuel cells remains difficult. The majority of these μFCs employ perfluorosulfonic acid polymer membranes (e.g., Nafion) whose integration via MEMS/IC-compatible techniques remains challenging. This particular issue has long prohibited true monolithic integration of micro-fuel cells for on-chip power generation.

As an alternative, laminar flow fuel cells (LFFCs), which simplify the micro-fuel cell architecture by omitting the proton exchange membrane (PEM), have been studied extensively [21,22]. These membraneless LFFCs utilize the characteristic laminar state of flows at the microscale to sustain the separation of coflowing fuel and oxidant streams in a single channel [23]. The diffusion along the interface is limited and hence fuel crossover is minimized while proton transport can still occur. The anode and cathode electrodes are typically positioned on opposing channel walls. This microfluidic fuel-cell configuration significantly reduces ohmic losses associated with the membrane as well as hydration/dehydration cycles and cathode flooding (i.e., water management) [22,23]. Moreover, by excluding the proton exchange membrane, the traditional μFC stack coalesces into a single substrate, enhancing the possibility of full on-chip monolithic integration with fabrication sequences tailored from MEMS and IC techniques. Using this concept, Tominaka et al. proposed a membraneless fuel cell with a monolithic structure, in which two electrodes were formed on a single substrate [24]. However, performance limitations were attributed to a limited oxygen supply through its passive air-breathing system. As an alternative, the utilization of liquid oxidants such as hydrogen peroxide (H_2O_2) [25,26], nitric acid (HNO_3) [27], and potassium permanganate ($KMnO_4$) [23,28,29] have been known to improve cathode kinetics and allow micro-fuel cells to produce higher power densities than with air-based approaches. Furthermore, liquid oxidants enable μFCs to perform in anaerobic applications such as submarine, sub-terrestrial and space missions [1].

Here we report on the fabrication of a planar, silicon-based monolithically integrated μLFFC, using standard MEMS and IC-compatible techniques. The μLFFC features a bridge-shaped microchannel cross-section to confine the diffusive liquid–liquid interface away from the electrode areas while minimizing crossover. The performance of this cell, operated with formic acid as the fuel and potassium permanganate as the oxidant, is presented.

2. μLFFC design concept and modeling

2.1. The importance of channel geometry

In typical LFFCs, anode and cathode catalyst-based electrodes are integrated on the opposite walls of a single rectangular channel. The design of a single flow field and the exclusion of a PEM are possible when streams coflow in the laminar state, self-constrained to their respective electrodes, while protons are able to migrate from anode to cathode. The only "separator" between the fuel and oxidant streams is essentially a liquid–liquid interface. Because the miscibility of the fuel and oxidant of choice is typically high, the liquid–liquid interface evolves into a diffusion (or mixing) zone which gradually increases in width as flow advances to the exit. Therefore, fuel crossover may occur and cell performance degrades. In such a scenario, strategic adjustments to the geometry of the main channel and upstream flow conditions allow for control over the width of the diffusion zone and the extent of crossover [30,31]. The width of the mixing zone can be predicted from the results of the scaling analysis [32]:

$$\Delta X = \left(\frac{DHy}{U_y} \right)^{1/3} \tag{1}$$

where D is the diffusivity of the species, H is the height of the channel, U_y is the average flow velocity, and y the distance the fluid flows downstream. Bazylak et al. simulated the effects of geometric variations to the main channel and determined that a higher aspect ratio (width:height) results in a thinner diffusive interface and improved fuel utilization [30]. Later, Chang et al. correlated improvements in cell performance to the degree of mixing as characterized by the Peclet number (Pe = U_yH/D) [31]. In their study, the diffusion transverse to the direction of flow (fuel crossover) was minimized by increasing the aspect ratio of the main channel, which involves a reduction in channel height (H). Consequently, both the average velocity and the Peclet number increase. Because increasing the aspect ratio minimizes the mixing width and crossover but also sacrifices electrode area, variations to the conventional rectangular channel geometry merit further exploration [33,34]. Here we introduce a μLFFC with a bridge-shaped microchannel geometry to minimize fuel-to-oxidant diffusive contact and isolate the corresponding mixing zone from the electrode areas while enabling efficient proton transport. Fig. 1 illustrates top and cross-sectional views of the new microchannel structure along with its geometric parameters. A bridge-shaped microchannel cross-section provides more walls for electrode integration, thus increasing the reactive area. This configuration enables anode and cathode electrochemical

Table 1
Summary of the performance of planar, monolithic, micro-fuel cells proposed for on-chip integration Only single cell performance is presented, unless otherwise noted.

Reference	Year	Reactant fuel/oxidant	Catalyst anode/cathode	Electrode area (cm^2)	OCP (V)	P_{max} (mW cm^{-2})	Current density at P_{max} (mA cm^{-2})
Lee et al. [19]	2002	H_2/O_2	Pt/Pt	5.0	~0.9[a]	~18[a]	~50[a]
Motokawa et al. [18]	2004	2 M CH_3OH/O_2-sat.	Pt–Ru/Pt	0.018	0.4	0.78	3.6
Min et al. [20]	2006	H_2/air	Pt/Pt	0.156	0.45	0.4	0.26
Xiao et al. [12]	2008	H_2/O_2	Pt–Ru/Pt–Ru	–	1.8[b]	10.5[b]	–
Tominaka et al. [24]	2008	2 M CH_3OH/air	Pt–Ru/Pd–Co	0.024	0.5	0.058[c]	0.33[c]
Shen et al. [39]	2009	1 M CH_3OH/0.01 M H_2O_2	Pt–Ru/Pt	0.048	0.46	3.0	11
This work		1 M HCOOH/0.144 M $KMnO_4$	Pd/none	0.024	1.35	26	28

[a] Values read of graph.
[b] Value corresponds to two serially connected cells (twin cell array).
[c] The authors reported a net power and current in (1.4 μW and 8 μA, respectively), which here is divided by the cathode area of 0.024 cm^2.

P.O. López-Montesinos et al. / Journal of Power Sources 196 (2011) 4638–4645
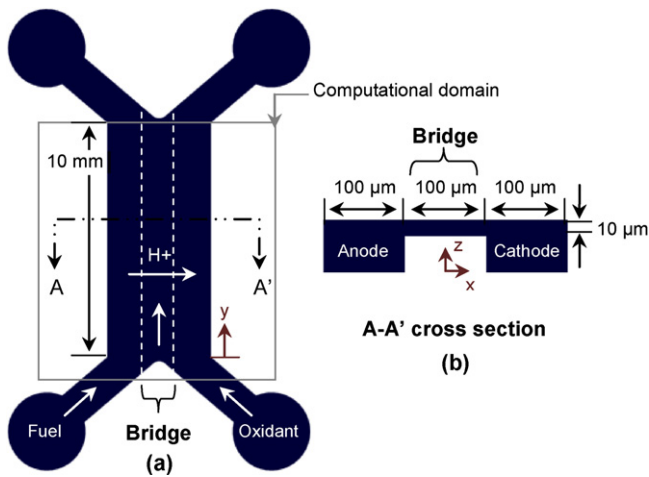

Fig. 1. Schematic illustration of the bridge-shaped microchannel structure and geometric parameters used in the simulations: (a) top view and (b) cross-sectional view.

reactions to proceed more efficiently as minimal or no interaction between the mixing region and the reaction zones is observed.

2.2. Mixing-zone model

To predict the behavior of the diffusion zone and to assess appropriate cell-design parameters and operating conditions, a three-dimensional (3D) model was developed using the commercial finite-element-method (FEM) software COMSOL Multiphysics 3.4 (COMSOL, Stockholm, Sweden). As illustrated in Fig. 1a, fuel (formic acid) and oxidant (potassium permanganate) streams enter separately through a Y-shaped entry, merge at the bridge location, and flow in parallel towards the exit. The computational domain consists of two sub-domains, namely, the anodic and cathodic flow channels. This allowed us to assign different physical properties and input conditions for each stream. Table 2 shows the physical properties and input parameters used in the simulations. The following assumptions were made to obtain simplified versions of the governing equations: (i) the density of the fluids (ρ) is constant; (ii) the fluids are Newtonian with constant viscosity (μ); (iii) the flow field is steady; (iv) the system experiences negligible body forces; (v) the cell operation is isothermal; and (vi) the mixing zone develops at a distant location from the electrode surface areas, so electrochemical reactions (depletion regions) have minimal impact on the local concentration gradient in the mixing zone, especially at low current densities. Also, because the fuel and oxidant solution are both dilute, we use the physical properties of pure water where necessary.

2.2.1. Governing equations

Using assumption (i), the general form of the mass-balance (continuity) equation for rectangular coordinates becomes:

$$\nabla \cdot \mathbf{u} = 0 \qquad (2)$$

where u is the velocity vector. Similarly, by applying assumptions (i) and (ii), a special case of the momentum-balance equation (Navier–Stokes) is obtained:

$$\rho \left(\frac{\partial \mathbf{u}}{\partial t} + \mathbf{u} \cdot \nabla \mathbf{u} \right) = -\nabla p + \mu \nabla^2 \mathbf{u} + p\mathbf{b} \qquad (3)$$

p denotes pressure and $\mathbf{b}$ is the body-force vector. Further, utilizing assumptions (iii) and (iv), the Navier–Stokes equation reduces to:

$$p(\mathbf{u} \cdot \nabla \mathbf{u}) = -\nabla p + \mu \nabla^2 \mathbf{u} \qquad (4)$$

Finally, under assumption (vi), the transport of species is of pure convective-diffusive nature and can be described by:

$$\nabla(-D\nabla c + c\mathbf{u}) = 0 \qquad (5)$$

where c is the concentration of a species and D indicates the corresponding diffusivity. Eqs. (2), (3) and (4) are coupled and simultaneously solved by applying system boundary conditions to obtain velocity and concentration fields.

2.2.2. Boundary conditions

The velocity solution is obtained by applying the following boundary conditions to Eqs. (2) and (3),

$$p = p_{in}, \quad p_{in} = \Delta p_{cell}; \text{ inlets} \qquad (6)$$

$$p = 0; \text{ outlets} \qquad (7)$$

when a zero-pressure condition is applied to the outlet, the inlet pressure (p_{in}) represents the cell pressure drop ($\triangle p_{cell}$). The no-slip condition is applied to all channel walls:

$$\mathbf{u} = 0; \text{ walls} \qquad (8)$$

Next, the velocity solution is coupled with Eq. (4) and the following boundary conditions apply:

$$c = c_{in}; \text{ inlets} \qquad (10)$$

where c_{in} is defined as the inlet concentration for the species of interest. A convective-flux condition is imposed to the outlet boundaries:

$$\mathbf{n}(-D\nabla c) = 0; \text{ outlets} \qquad (11)$$

while no mass transport can take place through walls:

$$\mathbf{n}(-D\nabla c + c\mathbf{u}) = 0; \text{ walls} \qquad (12)$$

2.2.3. Velocity field and mixing-zone analysis

Fig. 2 shows the magnitude of the velocity component in the flow direction (v_y) at a location of 5 mm ($y = 5$ mm) from the active channel entrance, where the catalyst coverage starts. The data represent a cross-sectional line which transverses the
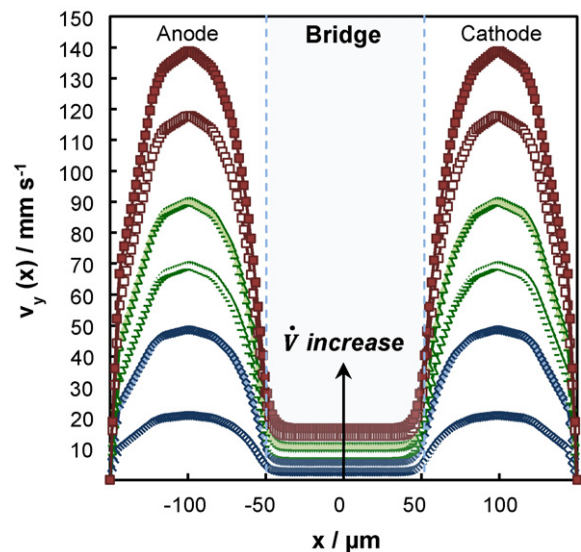

Fig. 2. Velocity component in the flow direction (v_y) at a location of 5 mm ($y = 5$ mm) from the cell active-channel entrance. The data represent a cross-sectional line which transverses the center of the bridge ($z = 45\,\mu$m) from the anodic channel outer side wall ($x = -150\,\mu$m) to the cathodic channel outer side wall ($x = 150\,\mu$m). The plot was generated for various flow rates $\dot{V} \in \{10, 20, 30, 40, 50, 60\}\,\mu$L min^{-1}, as indicated by the arrow.

center of the bridge ($z=45\,\mu m$) from the anodic channel outer side wall ($x=-150\,\mu m$) to the cathodic channel outer side wall ($x=150\,\mu m$). The plot was generated for various flow rates $\dot{V}\in\{10, 20, 30, 40, 50, 60\}\,\mu L\,min^{-1}$. At a specific input flow rate, a double-parabolic flow developed with a nearly constant low-velocity field in the bridge. Note that the local maxima observed do not represent the absolute maximum velocity of the flow field, because those occur approximately at the center of the two channels ($z=25\,\mu m$) for a given flow rate. The velocity field is fully symmetric because of the symmetry of the cell and the identical flow rates used in both channels. The low velocity field observed at the bridge is a result of the high proximity between the upper and lower walls at which the no-slip boundary condition applies. The magnitude of the downstream velocity in the bridge region increased from 4 to $20\,mm\,s^{-1}$ upon increasing the flow rates of the individual channels from 10 to $60\,\mu L\,min^{-1}$.
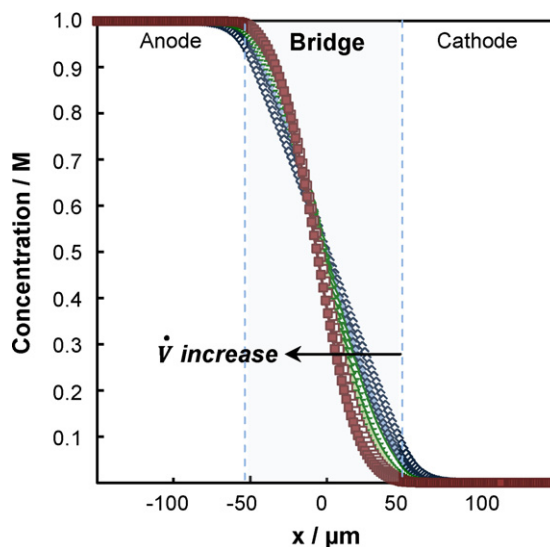
Fig. 3a captures the concentration profile when the cell is operated with 1 M HCOOH at a flow rate of $60\,\mu L\,min^{-1}$. This concentration field reveals the confinement of the mixing zone along the bridge for the entire flow domain. As listed in the assumptions (Section 2.2), due to the appreciable distance between the electrode walls and the point of liquid–liquid mergence (at the middle of the bridge for a 1:1 flowrate ratio), the depletion layers resulting from electrochemical reactions had a minimal impact on the concentration gradient in the mixing zone. Moreover, the Y-shape entry to the cell allows for a volume of unreacted liquids to merge initially at the bridge location and coflow along this catalyst-free zone towards the exit. This set of assumptions enabled us to exclude the reaction kinetics resulting in a simplified version of the model which allows the behavior of the diffusion zone to be studied independently. Fig. 3b illustrates x–z plane concentration snapshots at three locations downstream from the active cell entrance (1, 5 and 9 mm) when the inlet fuel concentration and flow rate were 1 M HCOOH and $60\,\mu L\,min^{-1}$, respectively. Note that the diffusion zone gradually increases in width as flow advances to the exit, but remains confined within bridge. Similarly, the oxidant
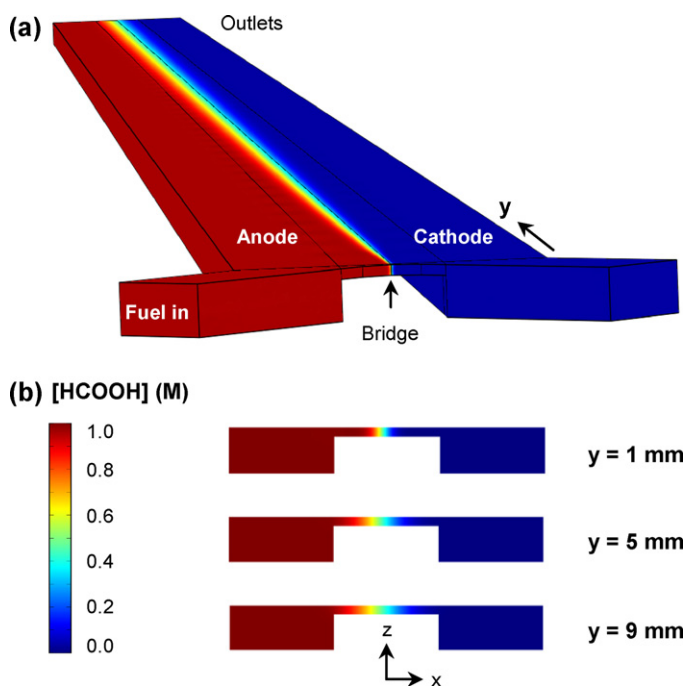
will exhibit diffusional broadening along the liquid–liquid interface (not shown here), but that profile will be close to identical to the concentration profile of the fuel (Fig. 3a) due to the virtually identical diffusions constants ($D_{HCOOH}=1.69\times10^{-9}\,m^2\,s^{-1}$ vs. $D_{KMnO_4}=1.63\times10^{-9}\,m^2\,s^{-1}$), and symmetry of the anode and cathode compartments.

The mixing zone width can be controlled by adjusting flow rates [30,31]. Fig. 4 depicts fuel-concentration profiles at a location of 5 mm ($y=5\,mm$) from the active cell entrance. Similar to Fig. 2, the data correspond to a cross-sectional line which transverses the center of the bridge ($z=45\,\mu m$) from the anodic channel outer side wall ($x=-150\,\mu m$) to the cathodic channel outer side wall ($x=150\,\mu m$). The concentration gradients are evaluated for different flow rates $\dot{V}\in\{10, 20, 30, 40, 50, 60\}\,\mu L\,min^{-1}$. In general, the immediate concentration gradient, which characterizes the diffusion zone, became steeper as the flow rate was increased. For instance, at a flow rate of $60\,\mu L\,min^{-1}$ this concentration gradient was well confined within the bridge. In contrast, at lower flow rates (i.e., $10\,\mu L\,min^{-1}$) the concentration gradient broadened and partially interfered with the inner anodic and cathodic channel side walls. To utilize the inner channel side walls for electrode (catalyst) integration interaction with the mixing zone must be avoided. The model suggests the use of higher flow rates to reduce the diffusion zone in order to achieve efficient electrode performance, which may improve fuel utilization. These results are in agreement with the scaling analysis given in Eq. (2), which indicates that increasing the average velocity results in a thinner diffusion zone. Returning to Fig. 2, the average velocity at the bridge location moderately increased proportionally to flow rate. Similarly, fuel crossover can be reduced by increasing the Peclet number [31]. According to our data (Fig. 2), Pe can be increased from $\sim1\times10^2$ to $\sim1\times10^3$ along the bridge using the aforementioned flowrate range. However, increasing Pe by increasing the mean velocity may cause the streams to deviate from steady state. Such an onset of hydrodynamic instability has been reported in laboratory experiments and hampers the performance of LFFCs significantly [23]. However, in this work the small dimensions of the bridge enables a more gradual development of the local velocity upon an increase in flow rate, which keeps Pe in a safe regime.

Fig. 3. Formic acid concentration profiles for a bridge-shaped microchannel geometry when fed with 1 M HCOOH at a flow rate of $60\,\mu L\,min^{-1}$: (a) 3D flow domain; (b) 2D captures with X–Z planes located at three different locations from the cell active-channel entrance (1, 5, and 9 mm in the downstream direction).

Fig. 4. Formic acid concentration gradients at a location of 5 mm ($y=5\,mm$) from the active cell entrance. The data correspond to a cross-sectional line which transverses the center of the bridge ($z=45\,\mu m$) from the anodic channel outer side wall ($x=-150\,\mu m$) to the cathodic channel outer side wall ($x=150\,\mu m$). The concentration gradients were evaluated for different flow rates. $\dot{V}\in\{10, 20, 30, 40, 50, 60\}\,\mu L\,min^{-1}$, as indicated by the arrow.
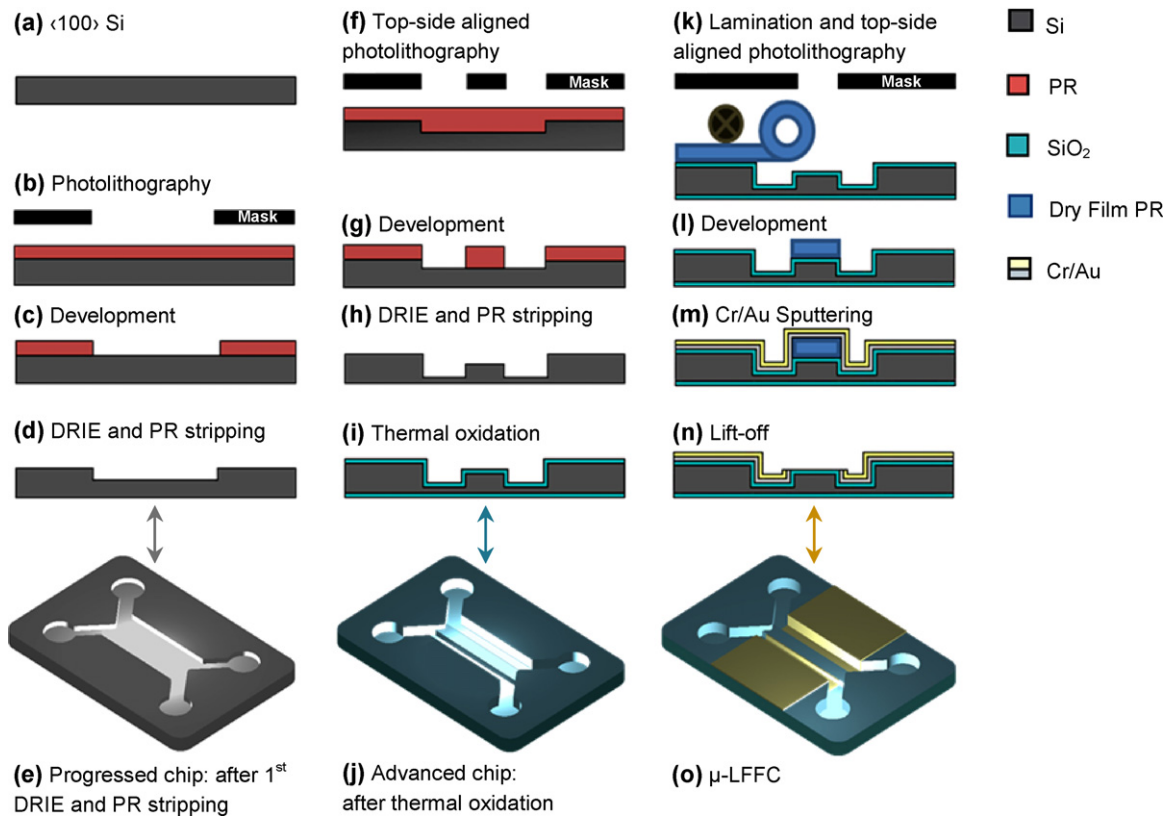
Fig. 5. μLFFC fabrication flow scheme: (a)–(e) 10 μm DRIE, (f)–(j) 50–75 μm DRIE (microchannels and feedholes) followed by Si thermal oxidation (SiO₂) and (k)–(o) integration of the Cr/Au current collectors.

3. Experimental

3.1. μLFFC fabrication and monolithic integration

The μLFFC was created and integrated in parallel using a set of MEMS and IC standard fabrication processes. In general, the procedure consisted of three UV-photolithographic steps followed by the corresponding additive or subtractive processes, as schematically illustrated in Fig. 5. In detail, a prime grade, p-type, ‹1 0 0›-oriented, double-sided polished silicon wafer (University Wafer) that is 100 mm in diameter with a resistivity of 1–10 Ω-cm (Fig. 5a) was spin coated with a positive-tone photoresist (AZ 4620, Clariant Co.) and exposed via photolithography using a mask aligner (Electronic Vision 420), Fig. 5b. The pattern was developed in diluted AZ400K (Clariant Co.) solution (Fig. 5c) and subsequently etched to 10 μm via inductively coupled plasma-deep reactive-ion etching (ICP-DRIE, Plasma-Therm SLR 770). The remaining photoresist was removed using resist stripper (AZ-400T, Clariant Co.), Fig. 5d. At the end of this fabrication sequence, a pattern composed of partially etched feedholes (1 mm in diameter) and microchannels (100 μm in width) along with a fully etched central bridging region (100 μm in width) was obtained. A 3D isometric projection of this substrate is shown in Fig. 5e. Similarly, to completely etch the feedholes and microchannels the advanced substrate was spin coated with AZ4620 photoresist and a second photolithographic exposure was executed using the aforementioned mask aligner (Fig. 5f). The new pattern was revealed with diluted AZ400K developer solution (Fig. 5g) and etched 40 μm (or 65 μm) deeper via ICP-DRIE. Residual photoresist was stripped off of the sample using AZ-400T solution (Fig. 5h). In addition, to ensure overall electrical insulation, a 5000-Å silicon dioxide film was thermally grown by consecutive dry and steam oxidation steps at 1100 °C using a manual oxidation furnace (Lindbergh-Tempress 8500), Fig. 5i. At this intermediate stage the whole μLFFC structure composed of anodic and cathodic microchannels connected via a partially opened central bridge has been completed (Fig. 5i). Finally, to integrate the current collectors, the structure was coated with a negative-tone dry-film photoresist (MX5030, DuPont) using a hot-roll laminator (Modulam 130, Think & Tinker, Ltd.) at 110 °C at a controlled feeding rate of 20.3 mm s^{-1}. A third photolithographic exposure was performed using a mask aligner (Fig. 5k) and the substrate was developed in 1 wt.% anhydrous sodium carbonate solution (Na₂CO₃, Think & Tinker, Ltd.) to generate the current collection pattern (Fig. 5l). A 200-nm gold layer was deposited via DC magnetron sputtering ($\sim$10^{-2} Torr of argon background pressure), preceded by deposition of a 40-nm chrome adhesion thin film (Fig. 5m). These Cr/Au current collectors were formed by lifting off the remaining dry-film photoresist in a 1.5 wt.% sodium hydroxide solution (NaOH, Aldrich) (Fig. 5n). The final monolithic μLFFC (single cell) is illustrated in Fig. 5o.

3.2. IC-compatible catalyst deposition

A pure Pd high-active-surface-area catalyst layer was selectively integrated into the anodic microchannel of the μLFFC using a previously reported IC-compatible electrodeposition method [16]. The potentiostatic deposition was performed at -2 V versus Ag/AgCl reference electrode (BAS) in a 0.08 M PdCl₂ bath (5 wt.% in 10 wt.% HCl, Aldrich) for 45 s via a computer interfaced potentiostat/galvanostat (Autolab PGSTAT 30, Eco-Chemie). In addition, field-emission environmental scanning electron microscopy (ESEM-FEG, Philips XL30, FEI) was performed to confirm in-channel deposition and to assess morphological details. No catalyst was required in the cathodic microchannel.
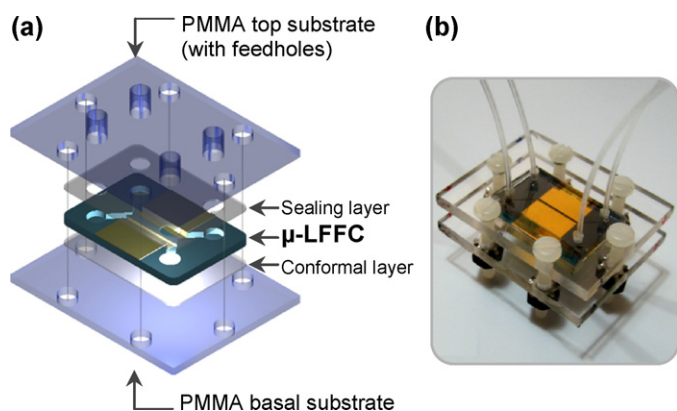
Fig. 6. (a) Schematic layout of the μLFFC experimental microfluidic fixture (PMMA top and basal substrates, PDMS sealing and conformal layers aligned to mechanically seal the chip); (b) photograph of the μLFFC secured in its microfluidic fixture for performance tests. The chip footprint is 26 mm × 18 mm.

3.3. μLFFC assembly and testing

An experimental microfluidic fixture (not a part of the monolithic design) was created for each fabricated μLFFC (Fig. 6). In brief, poly(methyl methacrylate) (PMMA) top and basal substrates along with polydimethylsiloxane (PDMS) sealing and conformal layers were aligned to mechanically secured the μLFFC using nylon screws. Conductive copper adhesive films (Compac/TriMas) were used to contact the Cr/Au current collectors.

The performance of the μLFFCs was assessed at room temperature and atmospheric pressure using the aforementioned potentiostat/galvanostat. The μLFFCs were fed with 1 M HCOOH/0.5 M H_2SO_4 (Aldrich/GFS Chemicals Powell) and 144 or 60 mM $KMnO_4$/0.5 M H_2SO_4 (Fisher) as the fuel and the oxidant, respectively, using a syringe infusion pump (11 Plus, Harvard Apparatus). As stated in Section 2, a 1:1 (fuel-to-oxidant) flow ratio was used with an input of 60 μL min^{-1}. Once the open-circuit potential (OCP) was determined, polarization curves were recorded by fixing the cell to a constant potential and reading the circuit current upon reaching steady-state conditions.

4. Results and discussion

4.1. μLFFC monolithic integration

One of the strategies used to achieve the monolithic integration of the μLFFC is to minimize the number of process steps needed for fabrication. For instance, feedholes (1 mm in diameter, Fig. 7a, left) were created concurrently with the first and second DRIE processes designated to etch the central bridging region and microchannels, respectively. This approach eliminates the need for a double-sided alignment process and a separate DRIE step often required to incorporate traditional all-through feedholes. Fig. 7a shows the μLFFC Y-shaped fluidic entry and microchannels connected via a central bridge where the fuel (1 M HCOOH) and oxidant (60–144 mM $KMnO_4$) streams are permitted to interface.

Similarly, minimizing the number of layers without hindering fuel cell performance simplifies the fabrication line and promotes cost-effective monolithic integration. Fig. 7b shows the incorporation of pure Pd high-active-surface-area catalyst into the anodic microchannel of the μLFFC using the technique described in Section 3.2, whereas no catalyst was needed in the cathodic microchannel. The corrugated (left) and smooth (right) surfaces correspond to the integrated Pd catalytic layer and bare Cr/Au cathodic current collector, respectively. The choice of a self-activated cathodic electron acceptor such as MnO_4^- as an alternative to catalyst-dependent oxidants such as oxygen eliminates the need to integrate an electroactive material into the cathodic microchannel. Compared to the dual anode-to-cathode catalyst system (*e.g.*, Pt–Ru/Pt) required in the majority of micro-fuel cell designs, the use of a single-anode catalyst system reduces the complexity of the steps required for precious-metal incorporation, which facilitates monolithic integration. Fig. 7c offers a magnified view of the electrodeposited Pd catalyst, which consists of a variety of spherical entities of round crystallites and fibrous surfaces. Further information on its structural characterization, electrocatalytic analysis, and its use for formic acid oxidation is available elsewhere [16]. Fig. 7d shows a cross-sectional view of the Pd catalyst-based anodic microchannel. SEM and profilometry (data not shown) suggested an average Pd catalyst-layer thickness of approximately 7 μm.
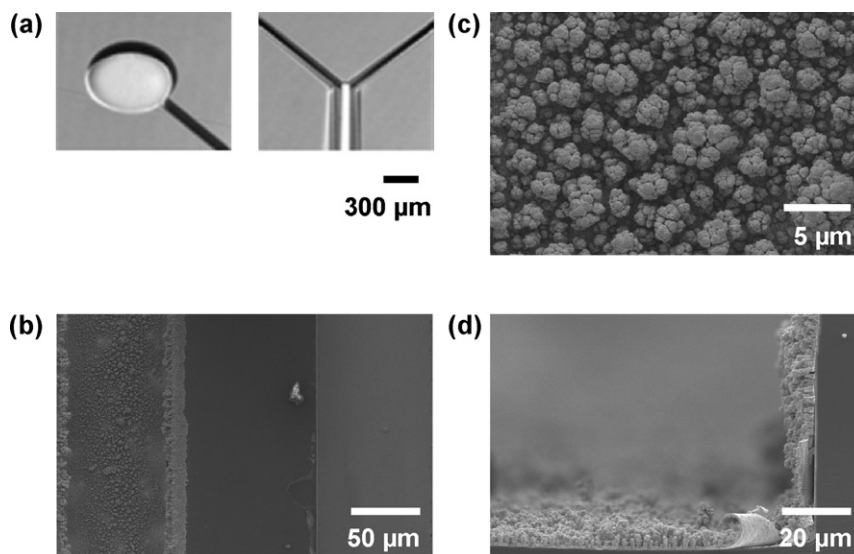
Fig. 7. Alpha-Step IQ camera and ESEM micrographs: (a) feedholes (left micrograph) and Y-shaped fluidic entry and microchannels after the second DRIE process (right micrograph); (b) electrodeposited Pd on Cr/Au sputtered anodic microchannel (left channel) and Cr/Au bare cathodic channel (right channel, no catalyst); (c) electrodeposited Pd on Cr/Au anodic microchannel at higher magnification; and (d) cross-sectional view of the Pd catalyst-based anodic microchannel.

4.2. μLFFC performance

The performance of two μLFFCs with bridge-shaped microchannel cross-sections (denoted Chip A and Chip B in this section) was assessed at room temperature and atmospheric pressure. Geometric parameters corresponding these chips were presented in Section 2 (Fig. 1). Chip A and B only differ in microchannel depth (50 vs. 75, respectively). The chips have identical footprints (length × width) of 26 mm × 18 mm (see the photograph in Fig. 6).

Chip A was operated with 1 M HCOOH/0.5 M H_2SO_4 and variable oxidant concentrations of 60 mM and 144 mM KMnO₄/0.5 M H_2SO_4, each at a flow rate of 60 μL min⁻¹. The unitary fuel-to-oxidant flow ratio ensured positioning of the liquid–liquid interface near the midline along the bridge location, as explained in Section 2. The polarization (open squares and circles) and power-density (filled squares and circles) curves of Chip A are shown in Fig. 8a. When the chip was operated at the low oxidant concentration of 60 mM KMnO₄, an open-circuit potential (OCP) of 1.4 V was attained. In addition, a maximum power density of 10.0 mW cm⁻² was obtained at a cell voltage and current density of 0.6 V and

(a) Chip A — 144 mM, 60 mM

(b) Chip B — 144 mM

Fig. 8. Polarization (open squares and circles) and power-density (filled squares and circles) curves for: (a) Chip A operating with 1 M HCOOH and two KMnO₄ concentrations (144 mM and 60 mM), all at flow rates of 60 μL min⁻¹; and (b) Chip B operating with 1 M HCOOH and 144 mM KMnO₄, each at a flow rate of 60 μL min⁻¹.

10.4 mA cm⁻², respectively. In contrast, when the same chip was operated at the higher oxidant concentration of 144 mM KMnO₄, an OCP value of 1.34 V was achieved. The 60 mV drop in OCP can probably be explained by the onset of oxidant crossover at the higher concentration. Under these conditions, chip A delivered a peak power density of 19.2 mW cm⁻² at a cell voltage and current density of 0.7 V and 27.4 mA cm⁻², respectively.
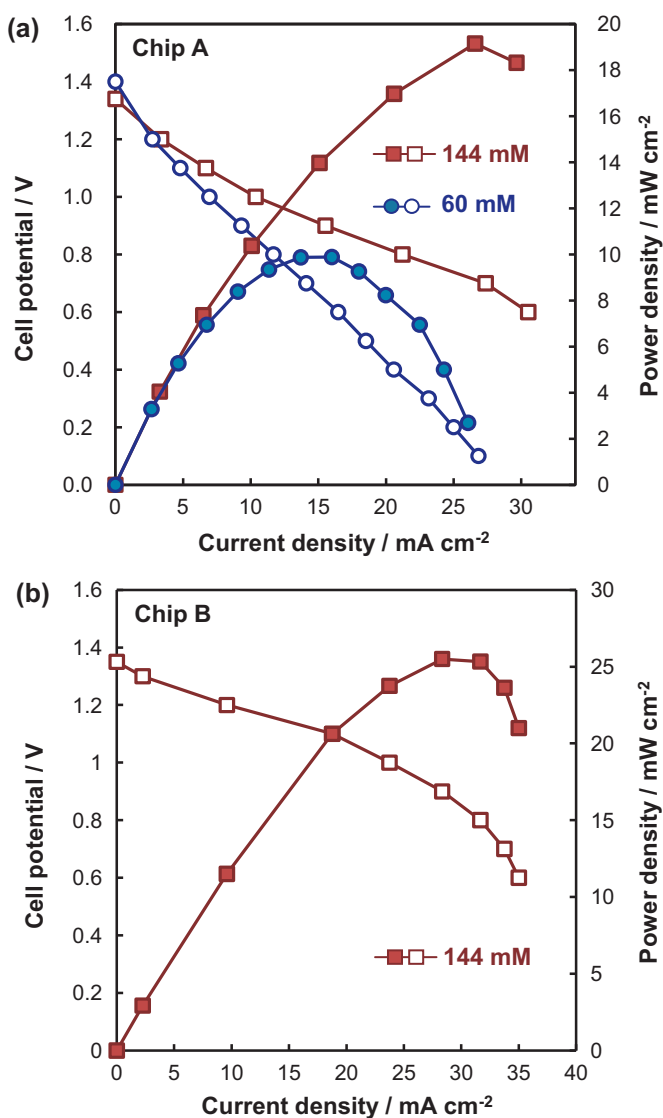
Similarly, Chip B was operated with 1 M HCOOH/0.5 M H_2SO_4 and a fixed oxidant concentration of 144 mM KMnO₄/0.5 M H_2SO_4, each at a of flow rate of 60 μL min⁻¹. The polarization (open squares) and power-density (filled squares) curves of Chip B are shown in Fig. 8b. An OCP of 1.35 V was attained, nearly identical to the OCP measured for Chip A. The power density reached a peak value of 25.5 mW cm⁻² at a cell voltage and current density of 0.9 V and 28.3 mA cm⁻², respectively.

The OCPs of formic acid (membraneless) LFFCs (of hybrid and monolithic integration) typically range from 0.6 V to 1.2 V for a variety of oxidants including potassium permanganate [23,28,29,35,36]. The reported increase in OCP herein may be due not only to the high redox potential of permanganate in acidic conditions ($E^0 = 1.70$ V) [37] but also to the minimal reactant crossover when employing a bridge-shaped microchannel configuration. The OCP values for the μLFFCs are >10% higher than those reported in literature for other formic acid/potassium permanganate cells [23,28,29].

In practical applications, a fuel cell is operated at a certain operating point that does not necessarily correspond to the maximum power density. Instead it is operated at a nominal power output that is a good compromise between cell efficiency, low capital cost, and operational stability [38]. In general, high voltage improves efficiency and lowers fuel consumption [38]. The μLFFCs studied here can be operated at nominal power (i.e., 0.6–0.7 V [38]) as well as at higher potentials, even exceeding 1 V due to their high OCP values.

When operated under the same experimental conditions, Chip B exhibited a ~25% higher maximum power density than Chip A (Fig. 8). Chip B has a deeper microchannel than Chip A (75 μm vs. 50 μm). The larger channel cross-sectional area of Chip B leads to a lower linear velocity at the inlet compared to Chip A (133 mm s⁻¹ vs. 200 mm s⁻¹). As modeled by Bazylak et al. [30], lowering inlet velocity in a low aspect-ratio rectangular channel geometry results in improved fuel utilization and superior performance due to an increase in reactant residence time. However, the extent to which velocity can be reduced depends upon maintaining a good compromise between fuel utilization, reduction of the depletion region [30,31] and the mixing zone, as discussed in Section 2.

The μLFFCs we report here exhibit higher peak power densities (P_{max}) than the previously reported planar, monolithic micro-fuel cells summarized in Table 1. In particular, compared to the most closely related design, the passive, membraneless, monolithic μFC with a similar electrode area reported by Tominaka et al. [24], our μLFFCs exhibited a more than 2 orders of magnitude increase in power density. However, energy losses associated with active reactant delivery (i.e., pumps) for systems with similar fluid flow resistances have been reported as ~100 μW [24]. This value is in agreement with the pressure drops we calculated for our cells operated at a flow rate of 60 μL min⁻¹ ($\triangle p_{cell}$ in Table 2). Even after taking into account these ancillary losses, the power output of our cells remains significantly higher. The marked increase in power density may be attributed to synergistic effects. The use of pure Pd catalyst facilitates the direct electro-oxidation of formic acid at low temperatures [16]. The direct pathway suppresses intermediate reaction steps which often lead to CO formation and associated with catalyst poisoning at the anode. Similarly, improved cathode kinetics is expected by using potassium permanganate due to a much lower activation barrier for electron transfer compared to

Table 2
Physical properties and input parameters used in the computations.

Parameter	Value
Fuel and oxidant density[a]	$1000 \, kg \, m^{-3}$
Fuel and oxidant viscosity[a]	$1 \times 10^{-3} \, N \, s \, m^{-2}$
Fuel and oxidant flow rate	$\{10, 20, 30, 40, 50, 60\} \, \mu L \, min^{-1}$
Fuel-to-oxidant flow rate ratio	1:1
Fuel and oxidant inlet velocity	$\{30, 70, 100, 130, 170, 200\} \, mm \, s^{-1}$
Cell pressure drop ($\triangle p_{cell}$)[a]	$\{2033, 4747, 6784, 8822, 11,540, 13,590\} \, N \, m^{-2}$
Fuel inlet concentration[a]	$1000 \, mol \, m^{-3}$ (1 M)
Diffusivity (HCCOOH)[a]	$1.69 \times 10^{-9} \, m^2 \, s^{-1}$

[a] Constants used to numerically solve mass, momentum, and species balance differential equations (2), (3) and (4).

oxygen [1]. Furthermore, the cell bridge-shaped architecture and operating conditions had a positive impact on cell performance by further reducing crossover (*i.e.*, preventing mixed potential) and enhancing reactant transport to the electrodes and their utilization as already elaborated upon in Section 2.

5. Conclusions

We have fabricated a planar, silicon-based, monolithically integrated μLFFC suitable as an on-chip power source. The MEMS-based, IC-compatible (*i.e.*, CMOS-compatible) fabrication process of these cells may facilitate their integration with electronics and controlling circuitry on the same chip. The bridge-shaped microchannel cross-section of these μLFFCs was shown to reduce fuel-to-oxidant interfacial contact, thereby minimizing reactant crossover. In addition, this geometry separates the mixing and reaction zones over the entire flow domain thereby enhancing reactant transport to the electrodes and improving fuel utilization. Appropriate cell-design parameters and operating conditions were obtained using a 3D diffusion-convection computational model. For the μLFFCs presented herein, the model suggested reactant flow rates ranging from 50 to 60 μL min^{-1} to enable the confinement of the mixing zone along the bridge and avoid its interaction with the electrode areas during operation. Experimentally, we observed high OCP values (1.34–1.35 V) which confirms the occurrence of minimal reactant crossover as a result of the bridge-shaped microchannel structure. The μLFFCs delivered peak power densities of 19 and 26 mW cm^{-2} when operated with 1 M HCOOH/0.5 M H$_2$SO$_4$ and 144 mM KMnO$_4$/0.5 M H$_2$SO$_4$ as fuel and oxidant, respectively, at a flowrate of 60 μL min^{-1}. Further refinement to the μLFFC design to optimize the proton aperture (*i.e.*, the bridge height) could further minimize cell resistance. On-chip integration of power sources may foster overall device miniaturization, weight and cost reduction, batch production, and reproducibility as desired for commercial applications. The planar, membraneless, monolithic, and CMOS-compatible micro-fuel cell design reported here may offer a solution for next generation of MEMS and consumer electronics whose highly integrated nature would benefit from on-chip incorporation of the power source.

Acknowledgements

References

[1] J.D. Morse, International Journal of Energy Research 31 (2007) 576–602.
[2] Y. Yamazaki, Electrochimica Acta 50 (2004) 663–666.
[3] S.C. Kelley, G.A. Deluga, W.H. Smyrl, AIChE Journal 48 (2002) 1071–1082.
[4] G.J. La O, H.J. In, E. Crumlin, G. Barbastathis, Y. Shao-Horn, International Journal of Energy Research 31 (2007) 548–575.
[5] S.F.J. Flipsen, Journal of Power Sources 162 (2006) 927–934.
[6] D. Dunn-Rankin, E.M. Leal, D.C. Walther, Progress in Energy and Combustion Science 31 (2005) 422–465.
[7] A. Kundu, J.H. Jang, J.H. Gil, C.R. Jung, H.R. Lee, S.H. Kim, B. Ku, Y.S. Oh, Journal of Power Sources 170 (2007) 67–78.
[8] N.T. Nguyen, S.H. Chan, Journal of Micromechanics and Microengineering 16 (2006) R1–R12.
[9] X. Yu, P.G. Pickup, Journal of Power Sources 182 (2008) 124–132.
[10] E. Kjeang, N. Djilali, D. Sinton, Journal of Power Sources 186 (2009) 353–369.
[11] M. Frank, G. Erdler, H.P. Frerichs, C. Müller, H. Reinecke, Journal of Power Sources 181 (2008) 371–377.
[12] Z. Xiao, C. Feng, P.C.H. Chan, I.M. Hsing, Sensors and Actuators B 132 (2008) 576–586.
[13] H.L. Maynard, J.P. Meyers, Journal of Vacuum Science and Technology B: Microelectronics and Nanometer Structures 20 (2002) 1287–1297.
[14] J.P. Meyers, H.L. Maynard, Journal of Power Sources 109 (2002) 76–88.
[15] J. Yeom, R.S. Jayashree, C. Rastogi, M.A. Shannon, P.J.A. Kenis, Journal of Power Sources 160 (2006) 1058–1064.
[16] R.S. Jayashree, J.S. Spendelow, J. Yeom, C. Rastogi, M.A. Shannon, P.J.A. Kenis, Electrochimica Acta 50 (2005) 4674–4682.
[17] C. Feng, Z. Xiao, P.C.H. Chan, I.M. Hsing, Electrochemistry Communications 8 (2006) 1235–1238.
[18] S. Motokawa, M. Mohamedi, T. Momma, S. Shoji, T. Osaka, Electrochemistry Communications 6 (2004) 562–565.
[19] S.J. Lee, A. Chang-Chien, S.W. Cha, R. O'Hayre, Y.I. Park, Y. Saito, F.B. Prinz, Journal of Power Sources 112 (2002) 410–418.
[20] K.B. Min, S. Tanaka, M. Esashi, Journal of Micromechanics and Microengineering 16 (2006) 505–511.
[21] R. Ferrigno, A.D. Stroock, T.D. Clark, M. Mayer, G.M. Whitesides, Journal of the American Chemical Society 124 (2002) 12930–12931.
[22] E.R. Choban, L.J. Markoski, J. Stoltzfus, J.S. Moore, P.J.A. Kenis, Proceedings of the 40th Power Sources Conference, Cherry Hill, NJ, 2002, pp. 317–320.
[23] E.R. Choban, L.J. Markoski, A. Wieckowski, P.J.A. Kenis, Journal of Power Sources 128 (2004) 54–60.
[24] S. Tominaka, S. Ohta, H. Obata, T. Momma, T. Osaka, Journal of the American Chemical Society 130 (2008) 10456–10457.
[25] G. Miley, N. Luo, J. Mather, E. Byrd, R. Burton, G. Hawkins, R. Gimlin, G. Kopec, P. Shrestha, G. Benavides, J. Laystrom, J. Rusek, T. Valdez, S. Narayanan, 8th Annual International Symposium Small Fuel Cells; Small Fuel Cells for Portable Applications, Washington, DC, 2006.
[26] T.I. Valdez, S.R. Narayanan, Proceedings of the Electrochemical Society, Pennington, NJ, 2001, pp. 265–273.
[27] A. Homa, 7th Annual International Symposium Small Fuel Cells, Washington, DC, 2006.
[28] M.H. Sun, G. Velve Casquillas, S.S. Guo, J. Shi, H. Ji, Q. Ouyang, Y. Chen, Microelectronic Engineering 84 (2007) 1182–1185.
[29] K.S. Salloum, J.R. Hayes, C. Friesen, J.D. Posner, Journal of Power Sources 180 (2008) 243–252.
[30] A. Bazylak, D. Sinton, N. Djilali, Journal of Power Sources 143 (2005) 57–66.
[31] M.H. Chang, F. Chen, N.S. Fang, Journal of Power Sources 159 (2006) 810–816.
[32] R.F. Ismagilov, A.D. Stroock, P.J.A. Kenis, G.M. Whitesides, H.A. Stone, Applied Physics Letters 76 (2000) 2376–2378.
[33] D.H. Ahmed, H.B. Park, H.J. Sung, Journal of Power Sources 185 (2008) 143–152.
[34] H.B. Park, D.H. Ahmed, K.H. Lee, H.J. Sung, Electrochimica Acta 54 (2009) 4416–4425.
[35] R.S. Jayashree, L. Gancs, E.R. Choban, A. Primak, D. Natarajan, L.J. Markoski, P.J.A. Kenis, Journal of the American Chemical Society 127 (2005) 16758–16759.
[36] J.L. Cohen, D.A. Westly, A. Pechenik, H.D. Abruna, Journal of Power Sources 139 (2005) 96–105.
[37] J. Li, Q. Fu, Q. Liao, X. Zhu, D.d. Ye, X. Tian, Journal of Power Sources 194 (2009) 269–274.
[38] F. Barbir, PEM Fuel Cells—Theory and Practice, Elsevier Academic Press, 2005.
[39] M. Shen, S. Walter, M.A.M. Gijs, Journal of Power Sources 193 (2009) 761–765.